

Article

Sustainable Synthesis of a Carbon-Supported Magnetite Nanocomposite Anode Material for Lithium-Ion Batteries

Hui Zeng, Jiahui Li, Haoyu Yin, Ruixin Jia, Longbiao Yu, Hongliang Li and Binghui Xu * 

Institute of Materials for Energy and Environment, College of Materials Science and Engineering, Qingdao University, Qingdao 266071, China

* Correspondence: xubinghuiqdu@qdu.edu.cn or xubinghuicsu@163.com

Abstract: Transition metal oxide magnetite (Fe_3O_4) is recognized as a potential anode material for lithium-ion batteries owing to its high theoretical specific capacity, modest voltage output, and eco-friendly character. It is a challenging task to engineer high-performance composite materials by effectively dispersing Fe_3O_4 crystals with limited sizes in a well-designed supporting framework following sustainable approaches. In this work, the naturally abundant plant products sodium lignosulfonate (Lig) and sodium cellulose (CMC) were selected to coprecipitate with Fe^{3+} ions under mild hydrothermal conditions. The Fe-Lig/CMC intermediate sediment with an optimized microstructure can be directly converted to the Lig/CMC-derived carbon matrix-supported Fe_3O_4 nanocomposite sample ($\text{Fe}_3\text{O}_4@\text{LigC/CC}$). Compared with the controlled $\text{Fe}_3\text{O}_4@\text{LigC}$ material, the $\text{Fe}_3\text{O}_4@\text{LigC/CC}$ nanocomposite provides superior electrochemical performance in the anode, which has inspiring specific capacities of 820.6 mAh g^{-1} after 100 cycles under a current rate of 100 mA g^{-1} and 750.5 mAh g^{-1} after 250 cycles, as well as more exciting rate capabilities. The biomimetic sample design and synthesis protocol closely follow the criteria of green chemistry and can be further developed in wider scenarios.

Keywords: magnetite; sodium lignosulfonate; sodium cellulose; green chemistry; lithium-ion batteries



Citation: Zeng, H.; Li, J.; Yin, H.; Jia, R.; Yu, L.; Li, H.; Xu, B. Sustainable Synthesis of a Carbon-Supported Magnetite Nanocomposite Anode Material for Lithium-Ion Batteries. *Batteries* **2024**, *10*, 357. <https://doi.org/10.3390/batteries10100357>

Academic Editor: Dino Tonti

Received: 11 September 2024

Revised: 8 October 2024

Accepted: 10 October 2024

Published: 11 October 2024



Copyright: © 2024 by the authors. Licensee MDPI, Basel, Switzerland. This article is an open access article distributed under the terms and conditions of the Creative Commons Attribution (CC BY) license (<https://creativecommons.org/licenses/by/4.0/>).

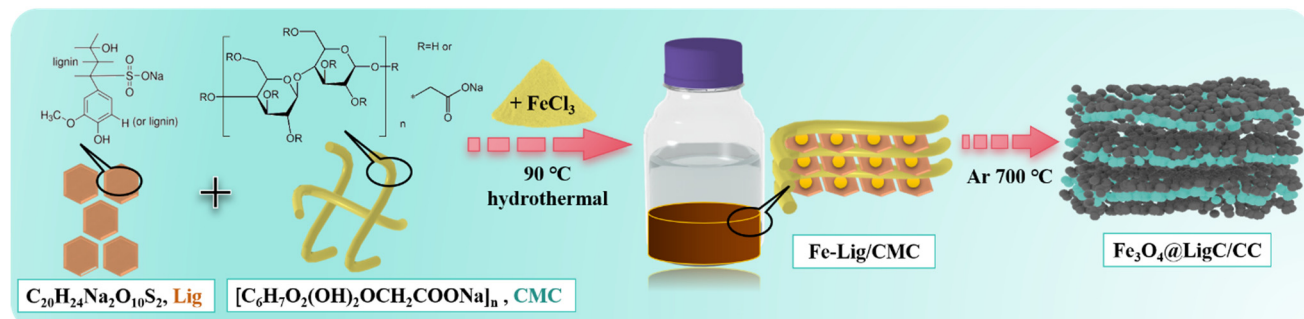
1. Introduction

Rechargeable lithium-ion batteries are predominantly utilized as an energy storage apparatus in modern society, and they play an extremely important role in relieving the pressure caused by the depletion of fossil fuels [1–4]. Upgrading the electrode materials with significantly improved lithium-ion storage capabilities is becoming pivotal in developing next-generation lithium-ion battery products. Compared with the current insertion-type graphitic anode materials, the conversion-type transition metal oxide magnetite (Fe_3O_4) has a much higher specific capacity as well as a modest voltage plateau and thus receives increasing research attention [5–7]. On the other hand, it is commonly recognized that the heavy volume expansion after lithiation and the poor inherent electric conductivity for the Fe_3O_4 anode are among the most critical problems before its commercialization.

In recent research, it has been confirmed that synthesizing Fe_3O_4 crystals with reduced particle sizes and further constructing a supportive carbon skeleton can effectively enhance their lithium-ion storage performance [8]. Moreover, these materials with attractive physical and chemical properties are being widely investigated in emerging fields, such as energy harvesting, photocatalysis, biosensing, biomedicine, and so on [9–12]. From the green chemistry viewpoint, it is particularly meaningful and challenging to engineer the corresponding composite materials with unique microstructures via simplified and sustainable approaches. In the natural plant kingdom, plant stems are generally recognized for their good mechanical strength and high flexibility, which enable them to stand up in a variety of environments. It has been revealed that the ordered crossing arrangement of the long-chain cellulose and smaller polymer lignin jointly contribute to the favorable

microstructure of these plant stems [13–15]. Moreover, cellulose and lignin are among the three most abundant available natural polymers, which means these materials have high potential for large-scale conversion and utilization. Therefore, they offer an alternative material design and engineering strategy following the bionic principles [16,17]. Sodium lignosulfonate (Lig) and sodium cellulose (CMC) are available products derived from natural lignin and cellulose, respectively. Both Lig and CMC feature good hydrophilicity due to their rich functional groups. Therefore, the structural advantages enable Lig and CMC to have good processibility in aqueous conditions, which means they can easily complex with transition metal ions to synthesize precursor samples [18]. In our previous work, CMC and Fe^{3+} ions were first employed as starting materials to synthesize a final porous carbon-supported Fe_3O_4 nanocomposite ($\text{Fe}_3\text{O}_4@\text{PC}$) using a two-step method [19]. However, due to the ineffective stabilization from the PC domains derived from the 1D CMC, the $\text{Fe}_3\text{O}_4@\text{PC}$ exhibited unsatisfactory electrochemical behaviors. Therefore, optimizing sample design and synthesis are challenging tasks in developing a sustainable strategy.

On the foundation above, as shown in Scheme 1, both Lig and CMC with different sizes and microstructures were jointly selected as carbon precursors to interact with Fe^{3+} ions in mild hydrothermal conditions. Taking advantage of the coordination capability with Fe^{3+} ions of Lig and CMC, an Fe-Lig/CMC intermediate sample with improved microstructure can be engineered. After a simple inert thermal treatment, the Fe-Lig/CMC can finally be converted to the Lig/CMC-derived carbon matrix-supported Fe_3O_4 nanocomposite sample ($\text{Fe}_3\text{O}_4@\text{LigC/CC}$). It is not surprising that the $\text{Fe}_3\text{O}_4@\text{LigC/CC}$ sample delivers significantly elevated lithium-ion storage performance compared with the controlled $\text{Fe}_3\text{O}_4@\text{LigC}$ sample. This work demonstrates a sustainable and scalable sample synthesis protocol using abundant, natural, plant-derived products as raw materials. Moreover, the $\text{Fe}_3\text{O}_4@\text{LigC/CC}$ sample can be considered for more feasible applications beyond the energy storage field.



Scheme 1. Schematic diagram of the engineering of the $\text{Fe}_3\text{O}_4@\text{LigC/CC}$ nanocomposite.

2. Experimental

2.1. Sample Synthesis

The chemicals were of analytical purity; they were purchased from the Sinopharm Company and used as received.

CMC (0.5 g) and Lig (0.5 g) were added to deionized water with uninterrupted stirring until a homogeneous suspension was formed in the first 4 h. After gradually adding the $\text{FeCl}_3 \cdot 6\text{H}_2\text{O}$ (2.0 g) aqueous solution into the reaction system, brown flocculent Fe-Lig/CMC sediment was gradually generated in the subsequent 6 h. The Fe-Lig/CMC intermediate sample was collected after water washing and following freeze-drying treatment, and then it was thermally treated in Ar at 700 °C for 2 h. Finally, the black $\text{Fe}_3\text{O}_4@\text{LigC/CC}$ powder sample could be synthesized.

The controlled $\text{Fe}_3\text{O}_4@\text{LigC}$ sample was fabricated following the same procedures used for the $\text{Fe}_3\text{O}_4@\text{LigC/CC}$ sample without using CMC in the raw materials.

2.2. Sample Characterization and Electrochemical Measurement

The detailed sample characterization and electrochemical measurement can be found in the supporting information file.

3. Results and Discussion

3.1. Engineer the $\text{Fe}_3\text{O}_4@\text{LigC/CC}$ Nanocomposite from Natural Products

The coprecipitation between Lig, CMC molecules, and Fe^{3+} ions is first triggered in mild hydrothermal conditions utilizing the coordination interaction, and the Fe-Lig/CMC intermediate sediment sample can be engineered. The well-dispersed Fe^{3+} ions in the Lig/CMC domain with rationally designed microstructure provide a good prerequisite for the final conversion of the Fe-Lig/CMC to the $\text{Fe}_3\text{O}_4@\text{LigC/CC}$ nanocomposite.

Figure 1a shows the XRD pattern of the $\text{Fe}_3\text{O}_4@\text{LigC/CC}$ nanocomposite. The sharp XRD diffraction peaks are strictly indexed by the crystalline Fe_3O_4 phase (PDF#19-0629). In addition, an obvious broad peak located near 26 degrees two theta could be ascribed to the LigC/CC carbonaceous supporting matrix. Further characterization information about $\text{Fe}_3\text{O}_4@\text{LigC/CC}$ was obtained from the Raman spectrum in Figure 1b. These peaks, located at 1333 and 1594 cm^{-1} , may be related to the D-band induced by the defective and disordered sp^3 carbon and the G-band induced by the ordered sp^2 carbon, respectively [20–22]. The calculated I_D/I_G value for the $\text{Fe}_3\text{O}_4@\text{LigC/CC}$ sample is 0.93 , which also means that the LigC/CC carbon skeleton is successfully transformed from the natural Lig and CMC products during further calcination.

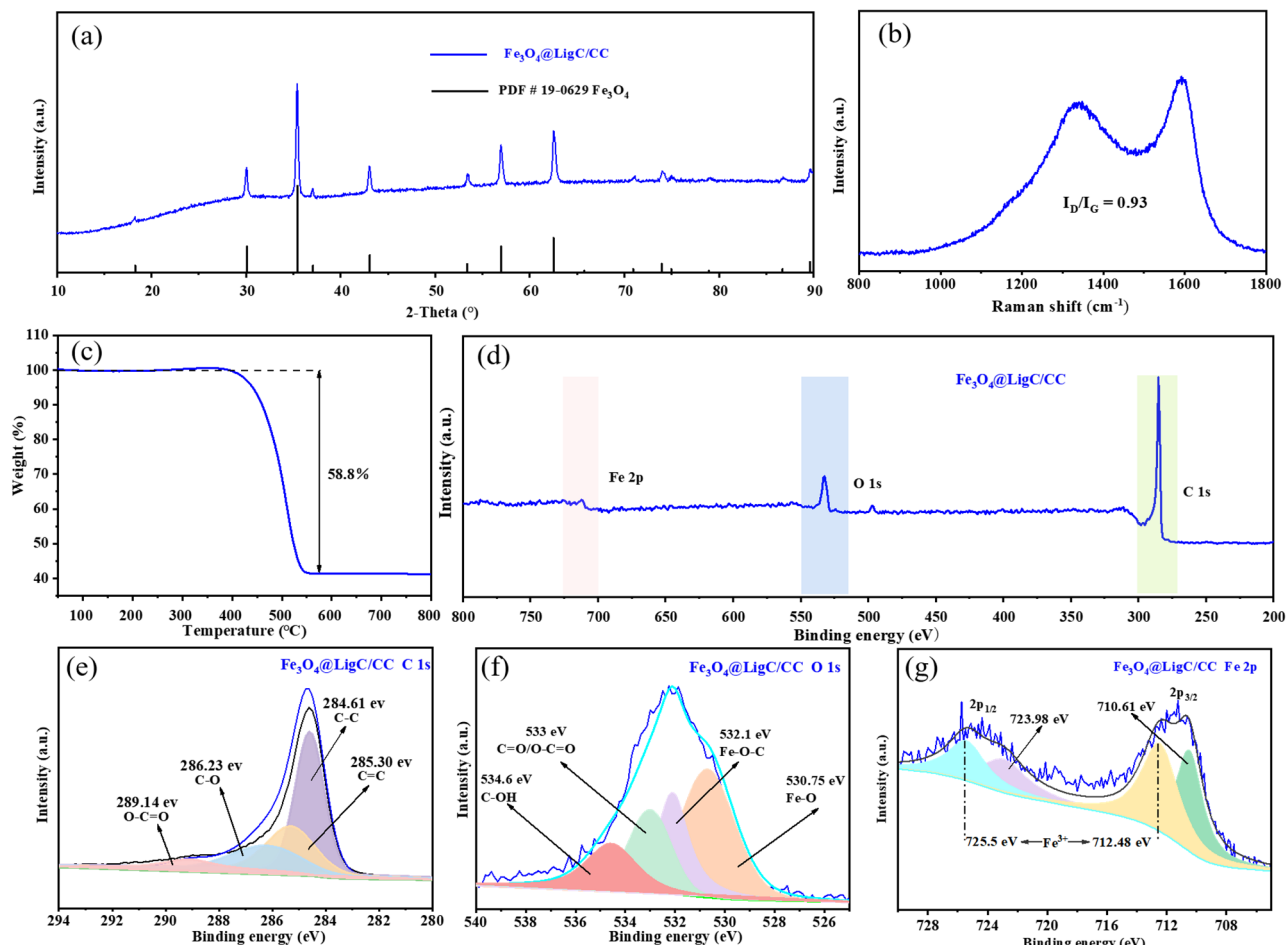


Figure 1. XRD pattern (a), Raman spectrum (b), TGA curve (c), survey XPS spectrum (d), high-resolution C 1s (e), O 1s (f), and Fe 2p (g), XPS spectra of the $\text{Fe}_3\text{O}_4@\text{LigC/CC}$ sample.

Figure 1c displays the TGA curve of the $\text{Fe}_3\text{O}_4@\text{LigC/CC}$ sample examined in air to determine the Fe_3O_4 and carbon content in the nanocomposite. The first negligible weight drop is usually explained by the elimination of the physically absorbed water, while the following slight weight increase from 250 to 350 °C can be ascribed to the further oxidation of Fe^{2+} to Fe^{3+} from the Fe_3O_4 crystals in air. In the temperature range of 400 to 550 °C, the rapid weight decrease is apparent. This result is caused by the removal of the LigC/CC carbonaceous supporting matrix. Moreover, it is also revealed that the overall mass drop is about 58.8% for the $\text{Fe}_3\text{O}_4@\text{LigC/CC}$ sample, leaving about 41.2% of the original weight for the residual in Fe_2O_3 form. According to the above result, it can be calculated that the Fe_3O_4 crystals and LigC/CC matrix occupy about 40.4% and 59.6% of the $\text{Fe}_3\text{O}_4@\text{LigC/CC}$ sample in weight, respectively.

According to the overall scanning XPS spectrum for the $\text{Fe}_3\text{O}_4@\text{LigC/CC}$ nanocomposite in Figure 1d, the existence of the three elements C, O, and Fe is validated. Figure 1e reveals the magnified C 1s spectrum, where the divided major peaks at 284.61 and 285.30 eV match with the graphitic C-C and C=C bonds, respectively [23], but the weak ones are highly related to the residual oxygen-contained radicals in the LigC/CC matrix. According to the O 1s spectrum in Figure 1f, the Fe-O peak located at 530.75 eV can be ascribed to lattice oxygen atoms from the Fe_3O_4 crystals, while the one at 532.1 eV can be assigned to the Fe-O-C bond connecting the Fe_3O_4 crystals and the carbon skeleton, implying good accommodation for the Fe_3O_4 crystals within the LigC/CC matrix [24]. The C=O/O-C=O peak at 533.0 eV and the C-OH peak at 534.6 eV show quite weakened strength, which means that the elimination of radicals in the LigC/CC matrix was not thorough [25]. According to the magnified Fe 2p spectrum in Figure 1g, the binding energies of 712.48 and 725.5 eV correspond to $\text{Fe } 2p_{3/2}$ and $\text{Fe } 2p_{1/2}$, respectively, showing an energy gap (ΔE) of 13.02 eV, and these are in good accordance with previously reported spectra of Fe^{2+} in Fe_3O_4 [26].

The microstructural and morphological information of the samples were first analyzed using the FESEM images. For the Fe-Lig/CMC intermediate sample in Figure 2a,b, nano-sized primary particles are aggregated to form the secondary micro-sized powder sample, and the individual Fe-Lig/CMC primary particles have similar sizes with clear space between them. This result means that the Lig and CMC molecules of different sizes have integrated with homogeneous dispersion of the Fe^{3+} ions, which is quite beneficial to the final conversion in the following thermal treatment. For the $\text{Fe}_3\text{O}_4@\text{LigC/CC}$ nanocomposite in Figure 2c,d, the micro-sized powder outlines are successfully inherited from the intermediate sample, while the Fe_3O_4 with similar-sized nanoparticles can be clearly seen in the carbon domains. In particular, no obvious excessive aggregation or over-exposure of these Fe_3O_4 nanocrystals can be verified, which is favorable for the elevation of the electrochemical performance of the $\text{Fe}_3\text{O}_4@\text{LigC/CC}$ anode material. By contrast, the controlled $\text{Fe}_3\text{O}_4@\text{LigC}$ sample in Figure 2e,f exhibits a quite different structure and morphology. Although the $\text{Fe}_3\text{O}_4@\text{LigC}$ sample exhibits a micro-sized particle outline, the Fe_3O_4 nanocrystals with a much larger size and a reduced quantity can be found in the intact pyrolytic carbon. The above structural differences of the $\text{Fe}_3\text{O}_4@\text{LigC/CC}$ and the controlled $\text{Fe}_3\text{O}_4@\text{LigC}$ samples verify that the joint utilization of Lig and CMC of different sizes as starting materials contributes to the optimization of the Fe_3O_4 nanocrystals and the carbon skeleton.

According to the TEM characterization of the $\text{Fe}_3\text{O}_4@\text{LigC/CC}$ nanocomposite in Figure 3a, Fe_3O_4 nanocrystals below 100 nm can be clearly observed in the carbon domain with good dispersion, which matches quite well with the FESEM characterization. The corresponding HRTEM characterization result for $\text{Fe}_3\text{O}_4@\text{LigC/CC}$ in Figure 3b demonstrates that the individual nanocrystal has an average lattice spacing of around 0.253 nm, which belongs to the (3 1 1) direction for Fe_3O_4 crystals. The Fe_3O_4 nanocrystals are well decorated on the carbon-supporting domain. According to the EDS analysis result for $\text{Fe}_3\text{O}_4@\text{LigC/CC}$ in Figure 3c, the Fe, O, and C elements are in good agreement from the

mapping with the corresponding atomic percentages of 4.59, 9.59, and 85.23, respectively. In addition, the trace amount of S element probably originates from the Lig product.

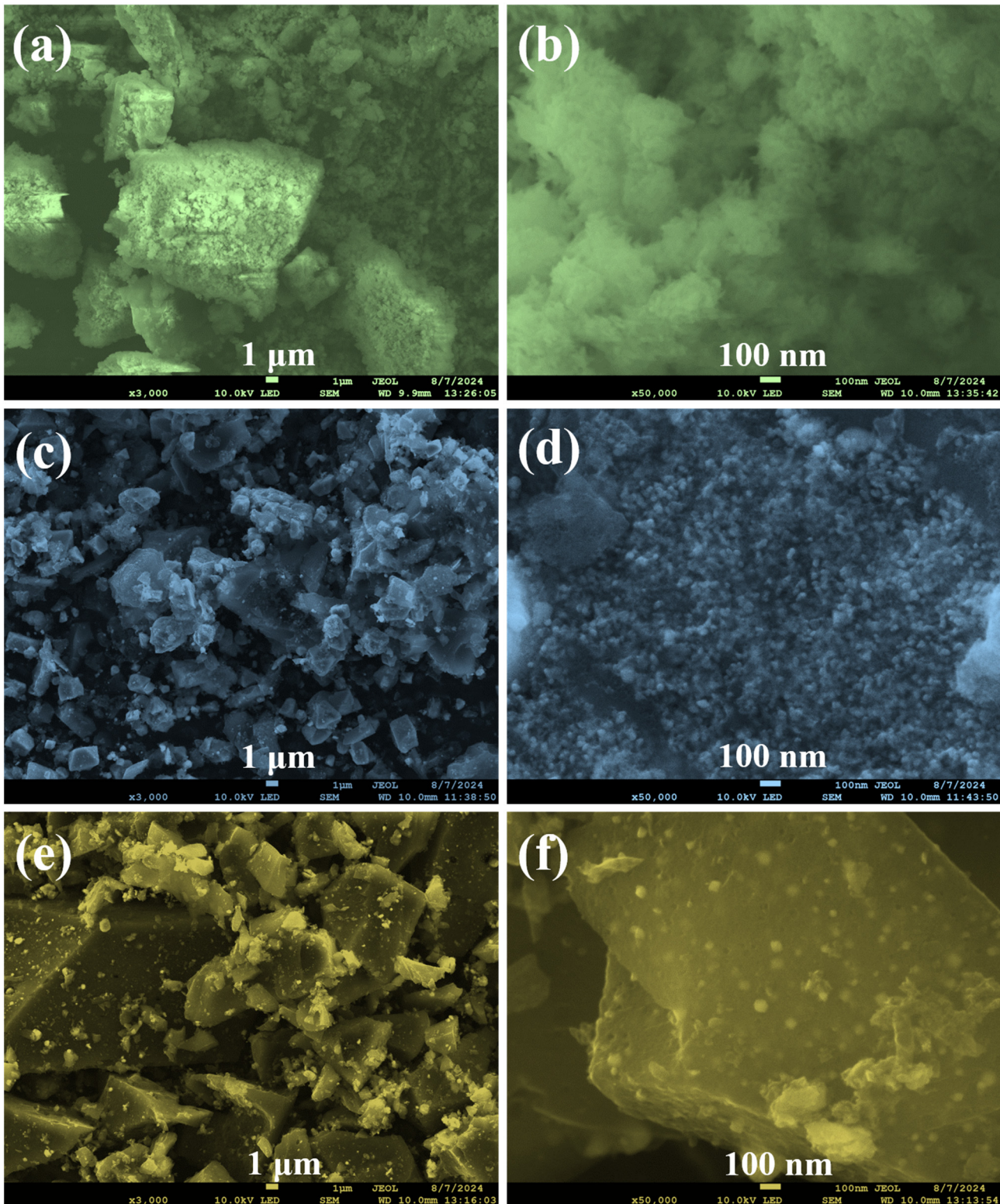


Figure 2. FESEM images of the Fe-Lig/CMC (a,b) and Fe₃O₄@LigC/CC (c,d) samples and the controlled Fe₃O₄@LigC sample (e,f) under corresponding magnifications.

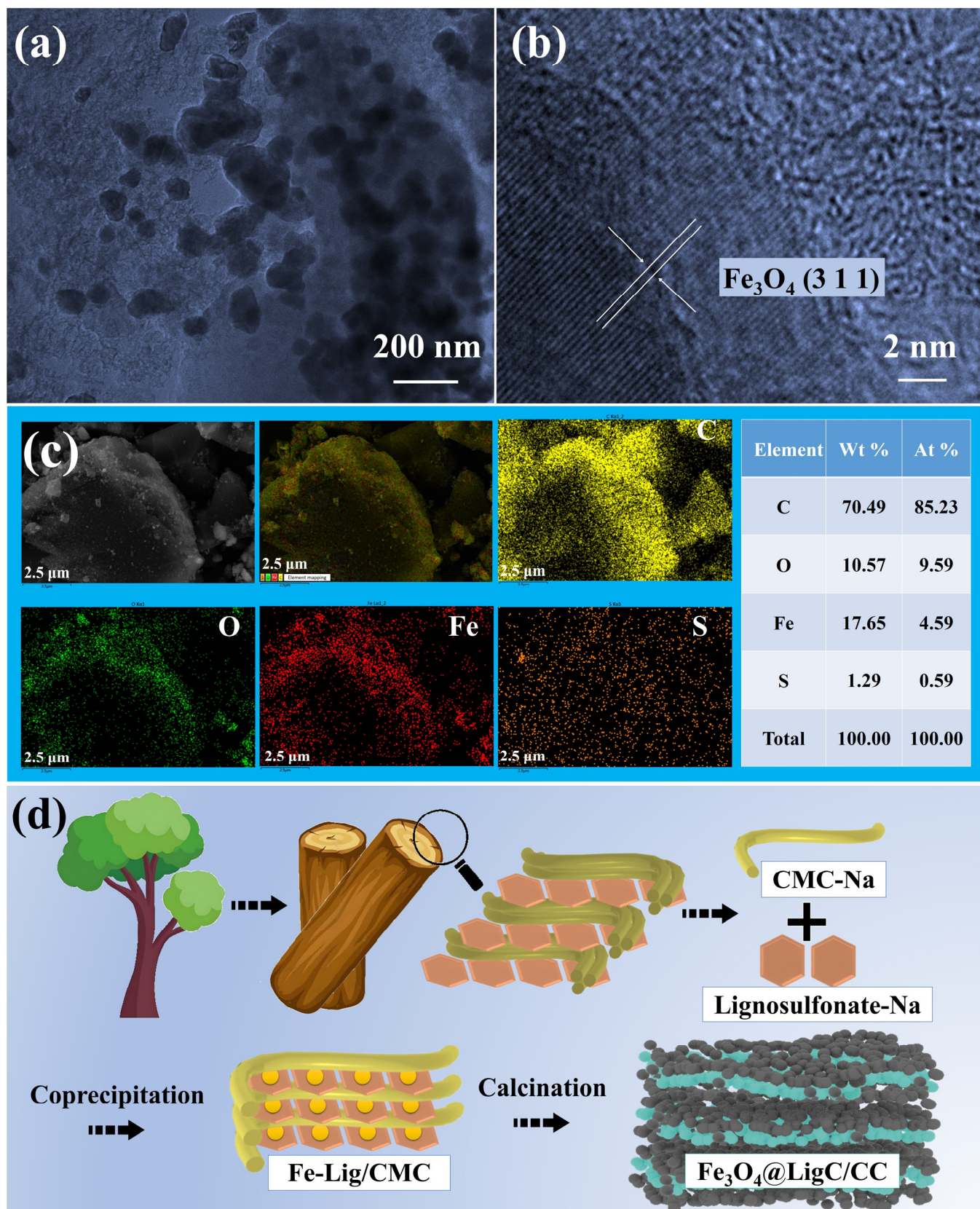


Figure 3. TEM (a) and HRTEM (b) images and the EDS testing result (c) of the $\text{Fe}_3\text{O}_4@\text{LigC/CC}$ sample; illustration of the sustainable and scalable sample design from plant-derived products (d).

Summarizing the above sample characterization results, the sample designing and engineering strategy in the work can be illustrated in Figure 3d. Following the principles of green chemistry, the natural plant-derived products Lig and CMC with different sizes are jointly employed as both carbon precursors and coordination organic materials, and water molecules are used as the reaction medium. At an ambient temperature, Fe^{3+} ions can be effectively complexed by the functional groups from both Lig and CMC, while the two organic molecules are reconstructed simultaneously. Therefore, the Fe-Lig/CMC intermediate sample with an optimized microstructure can be directly used to synthesize the final $\text{Fe}_3\text{O}_4@\text{LigC/CC}$ sample via a simple thermal treatment. In detail, the well-dispersed Fe^{3+} ions combine with the oxygen atoms to form iron oxide, which is generated due to the pyrolysis of the Lig/CMC precursor. The reduction capability of LigC/CC carbon atoms may convert the iron oxide phase to Fe_3O_4 crystals in the following stage, for which the crystal size is effectively controlled thanks to the atomic dispersion of the Fe^{3+} ions in the Lig/CMC matrix.

3.2. Lithium-Ion Storage Performances of the $\text{Fe}_3\text{O}_4@\text{LigC/CC}$ Nanocomposite

Figure 4a exhibits the CV testing result of the $\text{Fe}_3\text{O}_4@\text{LigC/CC}$ nanocomposite. In the first cycle, two small cathodic peaks can be seen at about 1.60 and 1.30 V. In addition, the most apparent cathodic one is situated around 0.51 V. The disappearance of these three peaks from the second cycle reveals the related reduction of the Fe_3O_4 species to metallic Fe domains and the accompanying generation of the irreversible solid electrolyte interphase (SEI) on the surface [27–30]. According to corresponding anodic scan curves, the two oxidizing peaks at 1.04 and 1.65 V indicate the reversible conversion of Fe phase to Fe_3O_4 . In the resting cathodic curves, the prominent reducing peak can be found at a higher voltage of about 0.97 V. The improved kinetics in the electrode contributes to the above shift, originating from the nano-sized effect of transition metal oxide electrodes for cycling [31]. Therefore, the electrochemical reaction for the Fe_3O_4 nanocrystals in the $\text{Fe}_3\text{O}_4@\text{LigC/CC}$ nanocomposite can be interpreted by the equation: $\text{Fe}_3\text{O}_4 + 8\text{Li}^+ + 8\text{e}^- \leftrightarrow 3\text{Fe} + 4\text{Li}_2\text{O}$. The outlines of the CV curves from the second cycle are nearly identical, demonstrating the satisfactory structure stability of the $\text{Fe}_3\text{O}_4@\text{LigC/CC}$ sample [32].

The testing curves in relation to the specific capacities and working voltage for $\text{Fe}_3\text{O}_4@\text{LigC/CC}$ are described in Figure 4b. In the starting discharging stage, the obvious long voltage platform belonging to the initial lithiation process could be identified near 0.7 V. This voltage platform shifts to a higher position at about 0.8 to 1.0 V for the resting ones. On the other hand, the corresponding charging parts demonstrate the main voltage platform between 1.5 and 2.0 V. These platforms significantly support the results of the CV testing. The $\text{Fe}_3\text{O}_4@\text{LigC/CC}$ nanocomposite can deliver the initial specific charging and discharging capacities of 936.6 and 1571.6 mAh g^{-1} , respectively, and the corresponding coulombic efficiency of 59.6% can be obtained. The irreversible capacity can be commonly attributed to the irreversible SEI generation in this cycle [33,34].

Figure 4c displays the low-current cycling performance of the $\text{Fe}_3\text{O}_4@\text{LigC/CC}$ nanocomposite at 200 mAh g^{-1} . It can be found that the specific charging and discharging capacities were 668.5 and 1037.4 mAh g^{-1} in the first cycle, respectively. Therefore, a higher coulombic efficiency of about 64.4% could be obtained compared with that at 1000 mAh g^{-1} . The $\text{Fe}_3\text{O}_4@\text{LigC/CC}$ composite delivers a gradual declining trend about the specific capacities for the first 15 cycles before rising for the following cycles. Stabilized specific capacity is delivered for the same sample and can be observed in the subsequent cycles, for which a high reversible one of 820.6 mAh g^{-1} after 100 cycles could be given. By contrast, the controlled $\text{Fe}_3\text{O}_4@\text{LigC}$ sample delivers a significantly inferior specific capacity at each cycle.

The rate capability for the $\text{Fe}_3\text{O}_4@\text{LigC/CC}$ nanocomposite can be seen in Figure 4d. With staged increases of current rates, the corresponding capacities drop in reverse. When tested by 100, 200, 500, 1000, 2000, and 5000 mA g^{-1} , mean capacities of about 922.5, 869.3, 793.3, 710.8, 602.0, and 381.4 mAh g^{-1} could be given in return, respectively. For the

last stage of 100 mAh g^{-1} , it is not surprising that the corresponding specific capacities significantly rise and remain stable, with a high average capacity of $1002.9 \text{ mAh g}^{-1}$. However, the control $\text{Fe}_3\text{O}_4@\text{LigC}$ sample has a much inferior electrochemical behavior in the rate testing.

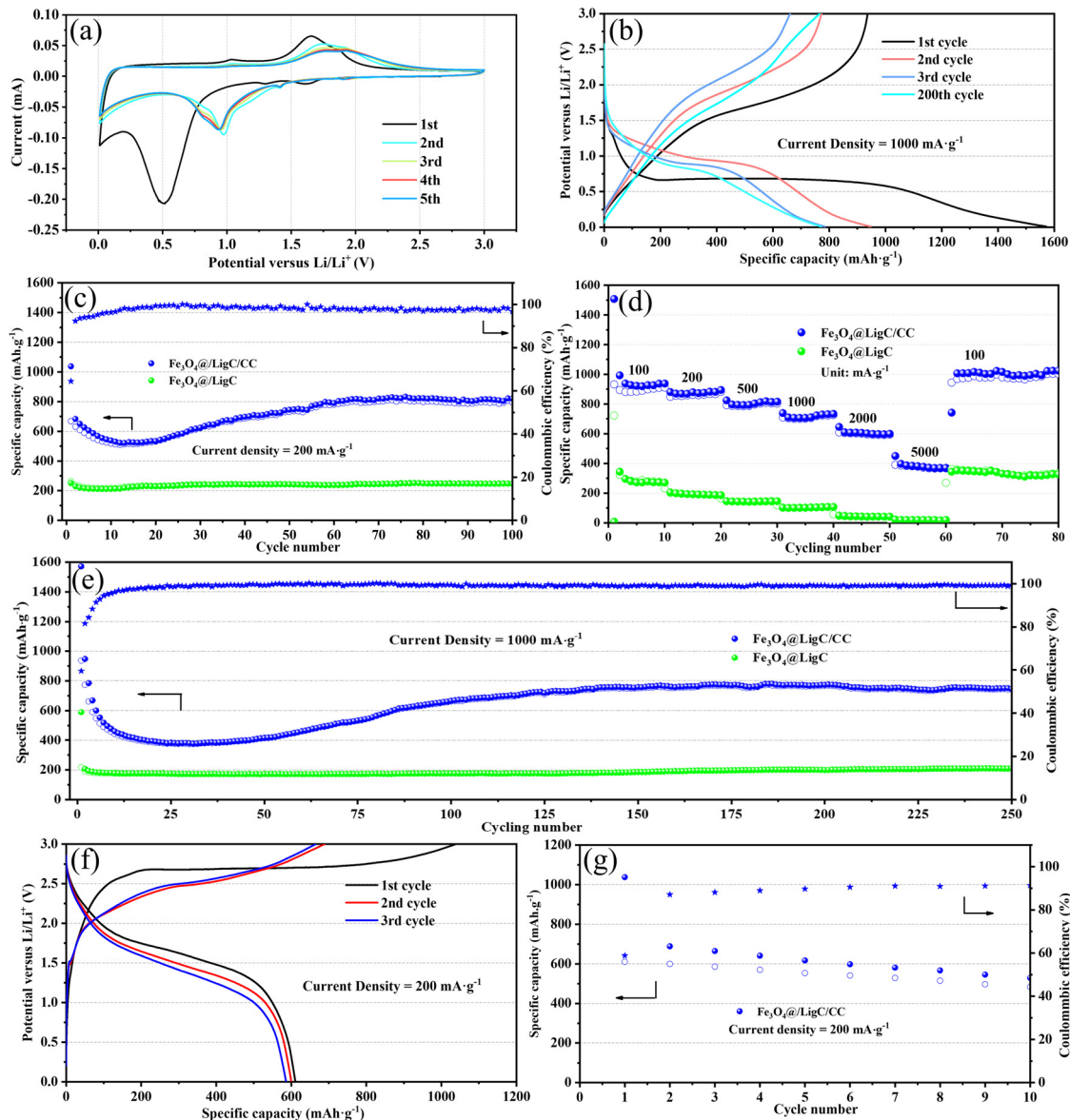


Figure 4. The CV curves for the initial five cycles (a) and charge and discharge voltage profile (b) of the $\text{Fe}_3\text{O}_4@\text{LigC/CC}$ sample; comparisons of the low-current cycling performances (c), rate capabilities (d), and high-current cycling performances (e) of the $\text{Fe}_3\text{O}_4@\text{LigC/CC}$ and $\text{Fe}_3\text{O}_4@\text{LigC}$ samples; charge/discharge voltage profile (f) and cycling performance (g) of the $\text{Fe}_3\text{O}_4@\text{LigC/CC}$ sample in $\text{Fe}_3\text{O}_4@\text{LigC/CC}/\text{LiFePO}_4$ full cell.

The high rate performances of the above two samples are compared in Figure 4e. Similar to the observations at 200 mAh g^{-1} , the $\text{Fe}_3\text{O}_4@\text{LigC/CC}$ nanocomposite shows a gradual capacity decline during the first 25 cycles before the capacity rises, which remains stable after about 150 cycles. More inspiringly, the $\text{Fe}_3\text{O}_4@\text{LigC/CC}$ sample delivers a specific capacity of 750.5 mAh g^{-1} after the continual 250 cycles, which is much higher than the value of 210.3 mAh g^{-1} for the $\text{Fe}_3\text{O}_4@\text{LigC}$ nanocomposite.

The testing curves in relation to the specific capacities and working voltage for $\text{Fe}_3\text{O}_4@\text{LigC/CC}$ in the $\text{Fe}_3\text{O}_4@\text{LigC/CC}/\text{LiFePO}_4$ full cell are illustrated in Figure 4f.

Similar to that in the half cell, this sample can deliver initial specific charging and discharging capacities of 1137.7 and 610.5 mAh g^{-1} , respectively, and a corresponding coulombic efficiency of 58.8% can be obtained. Moreover, a modest discharging voltage platform at about 1.5 V can be observed for the full cell. As can be seen in Figure 4g, a reversible capacity of 483.5 mAh g^{-1} can be maintained after 10 cycles, and the coulombic efficiency gradually rises to 91.7% for this sample.

From the above electrochemical testing results, it is obvious that the coulombic efficiency of the $\text{Fe}_3\text{O}_4@\text{LigC}/\text{CC}$ electrode gradually rises in the starting stages and stays stable in the remaining cycles. Moreover, the specific capacity drops at first and rises until it is stable in the subsequent testing. According to our previous research [34], there is additional metallic iron formation in this electrode during the starting cycles, which may lead to a decrease in the specific capacity and the coulombic efficiency. On the other hand, the in situ-formed iron atoms could contribute to the generation of a conductive polymer film at low voltages, which increases the specific capacity via pseudocapacitive behavior. In the last stage, the Fe domains gradually take part in the lithium-ion storage reaction caused by the gradually enhanced reaction environment. In addition, the coulombic efficiency increases accordingly and remains stable.

In Table 1, the key parameters for the lithium-ion storage of the carbon skeleton-supported Fe_3O_4 samples are clearly listed. Compared with the competitors, the $\text{Fe}_3\text{O}_4@\text{LigC}/\text{CC}$ nanocomposite could not only provide high and stable reversible capacity but also maintain a long cycling life. Particularly, the raw materials are naturally rich, and the whole sample preparation can be considered to possess the obvious merit of sustainability.

Table 1. Comparison of the lithium-ion storage performance of carbonaceous matrix-supported Fe_3O_4 materials.

Sample Name	Reversible Capacity (mAh g^{-1})	Cycle Number	Current Rate (mA g^{-1})	Year Published
$\text{Fe}_3\text{O}_4@\text{SnO}_7/\text{MXene}-10$ [35]	626.1	900	1000	2024
$\text{Fe}_2\text{O}_3@\text{Fe}_3\text{O}_4-5$ [36]	707.8	800	1000	2023
H-TiO ₂ /C/ $\text{Fe}_3\text{O}_4@\text{NiO}$ [37]	897.47	200	200	2023
$\text{Fe}_3\text{O}_4/\text{C}-500$ [38]	718	500	200	2023
Si-QDs/ $\text{Fe}_3\text{O}_4/\text{rGO}$ [39]	1367.1	80	100	2023
$\text{Fe}_3\text{O}_4@\text{void@N-Doped C-5}$ [40]	1222	100	200	2022
$\text{Fe}_3\text{O}_4@\text{C}$ [41]	291.7	300	1000	2022
$\text{Fe}_3\text{O}_4/\text{MWCNT}$ [42]	662	100	50	2022
$\text{Fe}_3\text{O}_4/\text{CNTS@C}$ [43]	612	200	1000	2021
$\text{Fe}_3\text{O}_4@\text{LigC}/\text{CC}$	820.6	100	200	
	750.5	250	1000	This work

The FESEM images of the prepared electrode were further used to examine the morphological change for the $\text{Fe}_3\text{O}_4@\text{LigC}/\text{CC}$ electrode. In Figure 5a,b, the micro-sized $\text{Fe}_3\text{O}_4@\text{LigC}/\text{CC}$ nanocomposite can be obviously seen in the fresh electrode, which has a slightly rough surface. The $\text{Fe}_3\text{O}_4@\text{LigC}/\text{CC}$ nanocomposite shows a similar microstructure to that in Figure 2d. After continual cycling 250 times, in Figure 5c,d, the $\text{Fe}_3\text{O}_4@\text{LigC}/\text{CC}$ electrode remains intact except for the slightly smoothed surface caused by SEI generation. In particular, the Fe_3O_4 nanocrystals can be clearly identified in this electrode. This result confirms the good stability of the $\text{Fe}_3\text{O}_4@\text{LigC}/\text{CC}$ electrode.

The Nyquist curves with the inset equivalent circuit model are shown in Figure 6a. The Nyquist diagrams are typically constituted by one semicircle as well as a connecting a straight line. The first intercept in the high-frequency region on the Z' axis refers to the inherent resistance in the cell (R_s). The next semicircle is located in the high-frequency and mid-frequency region, corresponding to the charge transfer resistor (R_{ct}). Lastly, the straight line in the low-frequency region corresponds to the Warburg impedance (Z_w), representing the lithium-ion diffusion resistance [44–46]. The obviously reduced R_{ct}

value of the $\text{Fe}_3\text{O}_4@\text{LigC}/\text{CC}$ composite electrode after cycling indicates improved charge transfer resistance and enhanced electronic conductivity.

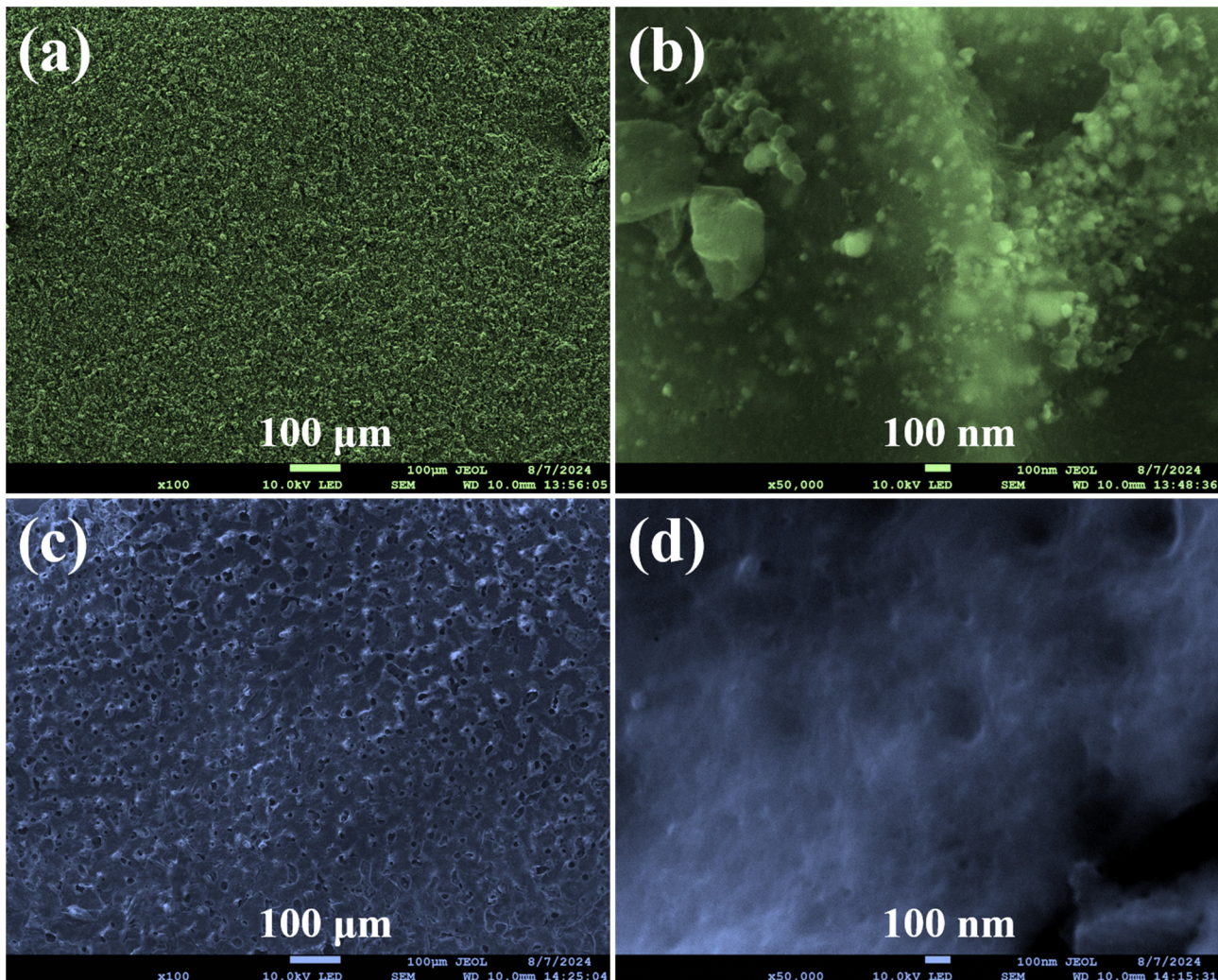


Figure 5. FESEM images of the $\text{Fe}_3\text{O}_4@\text{LigC}/\text{CC}$ electrode before cycling (**a,b**) and after 250 cycles (**c,d**) under the corresponding magnifications.

Cyclic voltammetry was further used to investigate the pseudocapacitive effect for the $\text{Fe}_3\text{O}_4@\text{LigC}/\text{CC}$ composite electrode. The series of CV curves in Figure 6b exhibits similar outlines at different current scanning rates. The kinetics of the nanocomposite could be measured on the basis of the equation regarding the peak current (i) and the scan rate (v) using the power-law formula $i = av^b$, in which b is a constant from plotting $\ln(i)$ against $\ln(v)$ [47]. A b value close to 0.5 implies that the diffusion process possesses the dominating position, while a b value close to 1.0 means that the pseudocapacitive process plays the main role [48]. Figure 6c reveals the plotting of $\ln(i)$ - $\ln(v)$ in $\text{Fe}_3\text{O}_4@\text{LigC}/\text{CC}$ electrode. The b values obtained by the cathodic and anodic peaks are 0.69 and 0.70, accordingly, indicating the co-existence of both pseudocapacitive and diffusion behaviors for the electrode [49]. The pseudocapacitive contributions can be further evaluated by the equation $i = k_1v + k_2v^{1/2}$ [50,51]. Therefore, the pseudocapacitive contribution in Figure 6d increases following the increase in the scanning rate of the $\text{Fe}_3\text{O}_4@\text{LigC}/\text{CC}$ electrode. The pseudocapacitive behavior of this electrode is probably triggered by the lithiation of Fe_3O_4 nanoparticles and adsorption on the unique LigC/CC carbon matrix [29,52,53]. Consequently, the accelerated surface lithium-ion storage reaction accompanied by the

reduced structural destruction of the nanocomposite lead to the superior electrochemical performance of the $\text{Fe}_3\text{O}_4@\text{LigC}/\text{CC}$ electrodes.

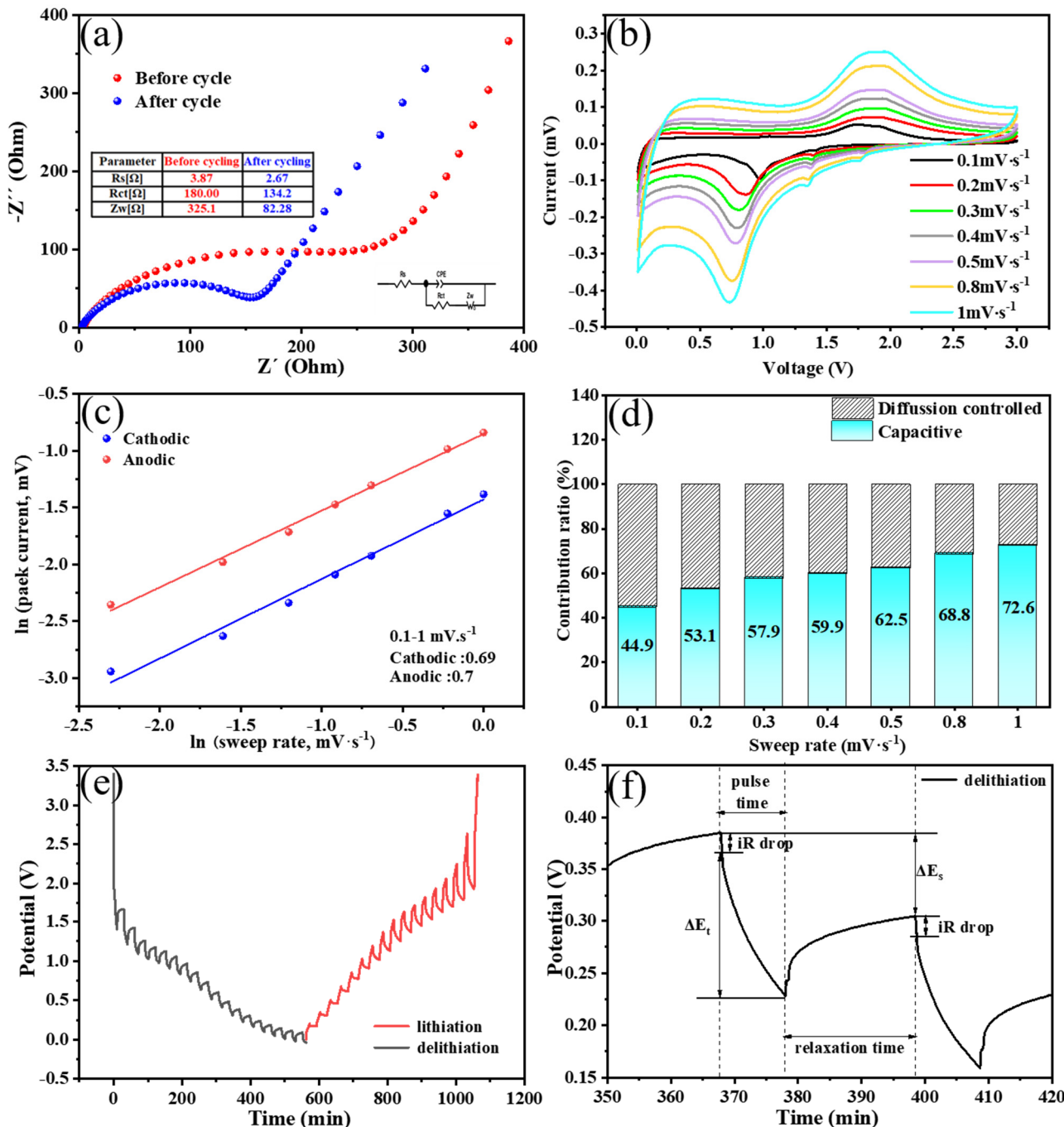


Figure 6. Nyquist plot of the $\text{Fe}_3\text{O}_4@\text{LigC}/\text{CC}$ electrode before cycling and after cycling with inset equivalent circuit obtained by fitting the EIS data (a); CV curves of the $\text{Fe}_3\text{O}_4@\text{LigC}/\text{CC}$ electrode at various scan rates from 0.1 to 1.0 $\text{mV}\cdot\text{s}^{-1}$ (b); the $\ln(i)$ - $\ln(v)$ plot (c); capacitive contribution and diffusion ratios at different rates (d); GITT curves of the $\text{Fe}_3\text{O}_4@\text{LigC}/\text{CC}$ electrode (discharge/charge state) (e); voltage (V vs Li^+/Li) versus time curve for one single GITT test (f).

The lithium-ion diffusion coefficient (D_{Li^+}) for the $\text{Fe}_3\text{O}_4@\text{LigC}/\text{CC}$ nanocomposite electrode is important for understanding charging and discharging behaviors. Hence, the constant current intermittent titration technique (GITT) is employed. The GITT curve of the $\text{Fe}_3\text{O}_4@\text{LigC}/\text{CC}$ electrode is illustrated in Figure 6e,f. According to Fick's second law,

the D_{Li^+} for $\text{Fe}_3\text{O}_4@\text{LigC}/\text{CC}$ can be obtained as follows: $D_{Li^+} = \frac{4L^2}{\pi\tau} \left(\frac{\Delta E_s}{\Delta E_t} \right)^2$, where τ is the pulse time, and ΔE_t and ΔE_s represent the gaps in the equilibrium potential and the current pulse, respectively [54–57]. The calculated results of LgD_{Li^+} show that the average value of D_{Li^+} in the lithiation state (discharge process) is $1.50 \times 10^{-12} \text{ cm}^2 \text{ s}^{-1}$, and the average value of D_{Li^+} in the delithiation state (charge process) is $1.98 \times 10^{-12} \text{ cm}^2 \text{ s}^{-1}$.

4. Conclusions

Following the principles of green chemistry and bionics, the natural plant-derived products Lig and CMC with different sizes are jointly employed as both carbon precursors and coordination organic materials to react with Fe^{3+} ions in mild hydrothermal conditions. The Fe-Lig/CMC intermediate sample with optimized microstructure is subsequently converted to the $\text{Fe}_3\text{O}_4@\text{LigC}/\text{CC}$ sample after calcination. The $\text{Fe}_3\text{O}_4@\text{LigC}/\text{CC}$ electrode shows more attractive specific capacities of 820.6 mAh g^{-1} after 100 cycles under a current rate of 100 mA g^{-1} and 750.5 mAh g^{-1} after 250 cycles, together with a good rate capability. The robust mechanical strength improves the electric and lithium-ion transferring condition, and the capacitive behaviors result in improved lithium-ion storage performance. This sustainable sample synthesis protocol and engineered $\text{Fe}_3\text{O}_4@\text{LigC}/\text{CC}$ nanocomposite can be further developed and have good prospects for application in wider fields.

Supplementary Materials: The following supporting information can be downloaded at: <https://www.mdpi.com/article/10.3390/batteries10100357/s1>.

Author Contributions: B.X. proposed the ideas, steps, and details of the experiment and wrote the article; most of the experiments were performed by H.Z.; and all the authors analyzed the data and discussed the conclusions. All authors have read and agreed to the published version of the manuscript.

Funding: This work was financially supported by the World-Class University and Discipline, the Taishan Scholar’s Advantageous and Distinctive Discipline Program, and the World-Class Discipline Program of Shandong Province.

Institutional Review Board Statement: Not applicable.

Informed Consent Statement: Not applicable.

Data Availability Statement: The data supporting the findings of this study are fully included within the main text of the article. Additional information or raw data may be available upon reasonable request from the corresponding author.

Conflicts of Interest: The authors declare no conflicts of interest.

References

1. Goodenough, J.B.; Park, K.S. The Li-ion rechargeable battery: A perspective. *J. Am. Chem. Soc.* **2013**, *135*, 1167–1176. [[CrossRef](#)] [[PubMed](#)]
2. Mihit, H.P.; Manikandan, P.; Vilas, G.P. Reserve lithium-ion batteries: Deciphering in situ lithiation of lithium-ion free vanadium pentoxide cathode with graphitic anode. *Carbon* **2023**, *203*, 561–570. [[CrossRef](#)]
3. Kebede, A.; Kalogiannis, T.; Van Mierlo, J.; Berecibar, M. A comprehensive review of stationary energy storage devices for large scale renewable energy sources grid integration. *Renew. Sustain. Energy Rev.* **2022**, *159*, 112213. [[CrossRef](#)]
4. Shia, C.; Wang, T.Y.; Liao, X.B.; Qie, B.Y.; Yang, P.F.; Chen, M.J.; Wang, X.; Srinivasane, A.; Cheng, Q.; Ye, Q.; et al. Accordion-like stretchable Li-ion batteries with high energy density. *Energy Storage Mater.* **2019**, *17*, 136–142. [[CrossRef](#)]
5. Cavers, H.; Molaiyan, P.; Abdollahifar, M.; Lassi, U.; Kwade, A. Perspectives on Improving the Safety and Sustainability of High Voltage Lithium-Ion Batteries Through the Electrolyte and Separator Region. *Adv. Energy Mater.* **2022**, *12*, 2200147–2200179. [[CrossRef](#)]
6. Chen, M.; Wang, E.; Liu, Q.; Guo, X.; Chen, W.; Chou, S.L.; Dou, S.X. Recent progress on iron- and manganese-based anodes for sodium-ion and potassium-ion batteries. *Energy Storage Mater.* **2019**, *19*, 163–178. [[CrossRef](#)]
7. Wang, Y.; Song, Y.; Xia, Y. Electrochemical capacitors: Mechanism, materials, systems, characterization and applications. *Chem. Soc. Rev.* **2016**, *45*, 5925–5950. [[CrossRef](#)]

8. Jia, R.X.; Yu, L.B.; Han, Z.Q.; Liu, S.; Shang, P.P.; Deng, S.Q.; Liu, X.H.; Xu, B.H. Synthesis of a MOF-derived magnetite quantum dots on surface modulated reduced graphene oxide composite for high-rate lithium-ion storage. *RSC Appl. Interfaces.* **2024**, *1*, 233–244. [[CrossRef](#)]
9. Xu, Z.; Yu, S.Y.; Xie, X.Y.; Li, Q.X.; Ding, L.; Chen, M.L.; Tu, J.; Xing, K.Y.; Cheng, Y.H. Target-triggered Fe_3O_4 @NPC-UCNPs assembly for photoactivatable biosensing of Aflatoxin B1. *Chem. Eng. J.* **2023**, *407*, 144028. [[CrossRef](#)]
10. Zhang, Y.F.; Qiu, L.G.; Yuan, Y.P.; Zhu, Y.J.; Jiang, X.; Xiao, J.D. Magnetic Fe_3O_4 @C/Cu and Fe_3O_4 @CuO core–shell composites constructed from MOF-based materials and their photocatalytic properties under visible light. *Appl. Catal. B-Environ.* **2014**, *144*, 863–869. [[CrossRef](#)]
11. Purna, K.B.; Gitashree, D.; Priyakshree, B.; Benjamin, L.O.; Manash, R.D. Fe_3O_4 quantum dots anchored on functionalized graphene: A multimodal platform for sensing and remediation of Cr (VI). *Chem. Eng. J.* **2023**, *474*, 145797. [[CrossRef](#)]
12. Wang, L.J.; Liu, F.H.; Pal, A.; Ning, Y.S.; Wang, S.; Zhao, B.Y.; Bradley, R.; Wu, W.P. Ultra-small Fe_3O_4 nanoparticles encapsulated in hollow porous carbon nanocapsules for high performance supercapacitors. *Carbon* **2021**, *179*, 327–336. [[CrossRef](#)]
13. Dühnen, S.; Betz, J.; Kolek, M.; Schmuck, R.; Winter, M.; Placke, T. Toward Green Battery Cells: Perspective on Materials and Technologies. *Small Methods* **2020**, *4*, 2000039. [[CrossRef](#)]
14. Wu, X.J.; Jiang, C.; Wang, J.; Pu, Y.; Ragauskas, A.; Li, S.; Yang, B. Lignin-derived electrochemical energy materials and systems. *Biofuels. Bioprod. Biorefin.* **2020**, *14*, 650–672. [[CrossRef](#)]
15. Norgren, M.; Edlund, H. Lignin: Recent advances and emerging applications. *Curr. Opin. Colloid Interface Sci.* **2014**, *19*, 409–416. [[CrossRef](#)]
16. Boerjan, W.; Ralph, J.; Baucher, M. Lignin Biosynthesis. *Annu. Rev. Plant Biol.* **2003**, *54*, 519–546. [[CrossRef](#)]
17. Feng, X.; Ren, D.; He, X.; Ouyang, M. Mitigating Thermal Runaway of Lithium-Ion Batteries. *Joule* **2020**, *4*, 743–770. [[CrossRef](#)]
18. Rinaldi, R.; Jastrzebski, R.; Clough, M.; Ralph, T.J.; Kennema, M.P.C.; Bruijnincx, B.M. Weckhuysen. Paving the Way for Lignin Valorisation: Recent Advances in Bioengineering, Biorefining and Catalysis. *Angew. Chem. Int. Ed. Engl.* **2016**, *55*, 8164. [[CrossRef](#)]
19. Lai, X.; Jin, C.; Yi, W.; Han, X.; Feng, X.; Zheng, Y.; Ouyang, M. Mechanism, modeling, detection, and prevention of the internal short circuit in lithium-ion batteries: Recent advances and perspectives. *Energy Storage Mater.* **2021**, *35*, 470–499. [[CrossRef](#)]
20. Pachfule, P.; Shinde, D.; Majumder, M.; Xu, Q. Fabrication of carbon nanorods and graphene nanoribbons from a metal–organic framework. *Nat. Chem.* **2016**, *8*, 718–724. [[CrossRef](#)]
21. Graf, D.; Molitor, F.; Ensslin, K.; Stampfer, C.; Jungen, A.; Hierold, C.; Wirtz, L. Spatially Resolved Raman Spectroscopy of Single- and Few-Layer Graphene. *Nano Lett.* **2007**, *7*, 238–242. [[CrossRef](#)] [[PubMed](#)]
22. Chen, W.F.; Li, S.R.; Chen, C.H.; Yan, L.F. Self-Assembly and Embedding of Nanoparticles by In Situ Reduced Graphene for Preparation of a 3D Graphene/Nanoparticle Aerogel. *Adv. Mater.* **2011**, *23*, 5679–5683. [[CrossRef](#)] [[PubMed](#)]
23. Shen, Z.; Xing, H.; Zhu, Y.; Ji, X.; Liu, Z.; Wang, L. Synthesis and enhanced microwave-absorbing properties of $\text{SnO}_2/\alpha\text{-Fe}_2\text{O}_3$ @RGO composites. *J. Mater. Sci. Mater. Electron.* **2017**, *28*, 13896–13904. [[CrossRef](#)]
24. Chandra, V.; Park, J.; Chun, Y.; Lee, J.W.; Hwang, I.C.; Kim, K.S. Water-Dispersible Magnetite-Reduced Graphene Oxide Composites for Arsenic Removal. *ACS Nano* **2010**, *4*, 3979–3986. [[CrossRef](#)]
25. Li, Y.; Wu, X.; Liu, C.; Wang, S.; Zhou, P.; Zhou, T.; Miao, Z.; Xing, W.; Zhuo, S.; Zhou, J. Fluorinated multi-walled carbon nanotubes as cathode materials of lithium and sodium primary batteries: Effect of graphitization of carbon nanotubes. *J. Mater. Chem. A* **2019**, *7*, 7128–7137. [[CrossRef](#)]
26. Li, H.H.; Saini, A.; Xu, R.Y.; Wang, N.; Lv, X.X.; Wang, Y.P.; Yang, T.; Chen, L.; Jiang, H.B. Hierarchical Fe_3O_4 @C nanofoams derived from metal–organic frameworks for high-performance lithium storage. *Rare Met.* **2020**, *39*, 1072–1081. [[CrossRef](#)]
27. Wei, Z.; Sarwar, S.; Azam, S.; Ahasan, M.R.; Voyda, M.; Zhang, X.; Wang, R. Ultrafast microwave synthesis of MoTe_2 @graphene composites accelerating polysulfide conversion and promoting Li_2S nucleation for high-performance Li-S batteries. *J. Colloid Interface Sci.* **2023**, *635*, 391–405. [[CrossRef](#)]
28. Wang, X.; Liu, X.; Wang, G.; Xia, Y.; Wang, H. One-dimensional hybrid nanocomposite of high-density monodispersed Fe_3O_4 nanoparticles and carbon nanotubes for high-capacity storage of lithium and sodium. *J. Mater. Chem. A* **2016**, *47*, 18532–18542. [[CrossRef](#)]
29. Cui, Y.; Feng, W.; Liu, W.; Li, J.; Zhang, Y.; Du, Y.; Li, M.; Huang, W.; Wang, H.; Liu, S. Template-assisted loading of Fe_3O_4 nanoparticles inside hollow carbon “rooms” to achieve high volumetric lithium storage. *Nanoscale* **2020**, *12*, 10816–10826. [[CrossRef](#)]
30. He, Q.; Chen, H.; Chen, X.; Zheng, J.; Que, L.; Yu, F.; Zhao, J.; Xie, Y.; Huang, M.; Lu, C.; et al. Tea-Derived Sustainable Materials. *Adv. Funct. Mater.* **2024**, *34*, 2310226. [[CrossRef](#)]
31. Xu, B.H.; Guan, X.G.; Zhang, L.Y.; Liu, X.W.; Jiao, Z.B.; Liu, X.H.; Hu, X.; Zhao, X.S. A simple route to preparing $\gamma\text{-Fe}_2\text{O}_3$ /RGO composite electrode materials for lithium-ion batteries. *J. Mater. Chem. A* **2018**, *6*, 4048–4054. [[CrossRef](#)]
32. Ma, C.; Shi, J.; Zhao, Y.; Song, N.J.; Wang, Y. A novel porous reduced microcrystalline graphene oxide supported Fe_3O_4 @C nanoparticle composite as anode material with excellent lithium storage performances. *Chem. Eng. J.* **2017**, *326*, 507–517. [[CrossRef](#)]
33. Zhang, W.; Li, X.; Liang, J.; Tang, K.; Zhu, Y.; Qian, Y. One-step thermolysis synthesis of two-dimensional ultrafine Fe_3O_4 particles/carbon nanonetworks for high-performance lithium-ion batteries. *Nanoscale* **2016**, *8*, 4733–4741. [[CrossRef](#)] [[PubMed](#)]

34. Kong, X.L.; Shan, L.; Zhang, R.; Bao, S.C.; Tu, M.Y.; Jia, R.X.; Yu, L.B.; Li, H.; Xu, B.H. Controllable engineering magnetite nanoparticles dispersed in a hierarchical amylose derived carbon and reduced graphene oxide framework for lithium-ion storage. *J. Colloid Interface Sci.* **2022**, *628*, 1–13. [CrossRef] [PubMed]
35. Hu, G.; Zhong, K.; Yu, R.; Liu, Z.; Zhang, Y.; Wu, J.; Zhou, L.; Mai, L. Enveloping SiO_x in N-doped carbon for durable lithium storage via an eco-friendly solvent-free approach. *J. Mater. Chem.* **2020**, *8*, 13285–13291. [CrossRef]
36. Duan, X.; Liu, J.Q.; Lv, F.S.; Liu, T.; Cui, W.B.; Wang, J.; Wang, Q.; Yuan, S. 3D porous structure Fe₃O₄@SnO₂/MXene composites with enhanced electrochemical performance for lithium ion battery anode. *J. Energy Storage.* **2024**, *86*, 111308. [CrossRef]
37. Lv, X.X.; Zhang, Y.; Lin, W.; Yang, A.W.; Liang, J. Facile synthesis of Fe₃O₄ ultrathin layer coated Fe₂O₃ composite anode for enhanced lithium-ion storage. *J. Electroanal. Chem.* **2023**, *947*, 117758. [CrossRef]
38. Wu, Q.C.; Qiu, S.; Yin, M.; Li, R.; Wang, Y.; Jin, D.Q.; Yang, R.H.; Yong, D.M.; Xie, W. Hydrogenated titanium dioxide modified core-shell structure Fe₃O₄@NiO for lithium-ion battery anode material. *Ionics* **2023**, *29*, 2227–2240. [CrossRef]
39. Li, M.; Ma, W.; Tan, F. Fe₃O₄@C-500 anode derived by commercial ammonium ferric citrate for advanced lithium ion batteries. *J. Power Sources* **2023**, *574*, 233146. [CrossRef]
40. Hu, W.; He, K.; Wu, S. Ordered sandwich silicon quantum dot/Fe₃O₄/reduced graphene oxide architectures for high-performance lithium-ion batteries. *J. Alloy Compd.* **2023**, *943*, 168947. [CrossRef]
41. Wang, J.; Hu, Q.; Hu, W. Preparation of hollow core-shell Fe₃O₄/nitrogen-doped carbon nanocomposites for lithium-ion batteries. *Molecules* **2022**, *27*, 396. [CrossRef] [PubMed]
42. Huang, J.; Dai, Q.; Cui, C. Cake-like porous Fe₃O₄@C nanocomposite as high-performance anode for Li-ion battery. *J. Electroanal. Chem.* **2022**, *918*, 116508. [CrossRef]
43. Sumit, R.S.; Jagannatham, M.; Gautam, R.; Rao Rikka, V.; Prakash, R.; Mallikarjunaiah, K.J.; Srinivas Reddy, G. A facile synthesis of raspberry-shaped Fe₃O₄ nanoaggregate and its magnetic and lithium-ion storage properties. *Mater. Sci. Eng. B Adv.* **2022**, *282*, 115771. [CrossRef]
44. Xu, J.L.; Zhang, X.; Miao, Y.X.; Wen, M.-X.; Yan, W.-Y.; Lu, P.; Wang, Z.-R.; Sun, Q. In-situ plantation of Fe₃O₄@C nanoparticles on reduced graphene oxide nanosheet as high-performance anode for lithium/sodium-ion batteries. *Appl. Surf. Sci.* **2021**, *546*, 149163. [CrossRef]
45. Ding, R.; Zhang, J.; Qi, J.; Li, Z.; Wang, C.; Chen, M. N-Doped Dual Carbon-Confined 3D Architecture rGO/Fe₃O₄/AC Nanocomposite for High-Performance Lithium-Ion Batteries. *ACS Appl. Mater. Interfaces* **2018**, *10*, 13470–13478. [CrossRef]
46. Xie, Y.; Qiu, Y.; Tian, L.; Liu, T.; Su, X. Ultrafine hollow Fe₃O₄ anode material modified with reduced graphene oxides for high-power lithium-ion batteries. *J. Alloys Compd.* **2022**, *894*, 162384. [CrossRef]
47. Li, H.; Wang, J.; Li, Y.; Zhao, Y.; Tian, Y.; Kurmanbayeva, I.; Bakenov, Z. Hierarchical sandwiched Fe₃O₄@C/Graphene composite as anode material for lithium-ion batteries. *J. Electroanal. Chem.* **2019**, *847*, 113240. [CrossRef]
48. Yin, L.; Gao, Y.J.; Jeon, I.; Yang, H.; Kim, J.P.; Jeong, S.Y.; Cho, C.R. Rice-panicle-like γ-Fe₂O₃@C nanofibers as high-rate anodes for superior lithium-ion batteries. *Chem. Eng. J.* **2019**, *356*, 60–68. [CrossRef]
49. Yan, Y.; Lu, X.; Li, Y.J.; Song, J.Q.; Tian, Q.; Yang, L.; Sui, Z. Dispersive Fe₃O₄ encapsulated in porous carbon for high capacity and long-life anode of lithium-ion batteries. *J. Alloys Compd.* **2022**, *899*, 163342. [CrossRef]
50. Ma, Q.; Zhao, Z.Q.; Zhao, Y.; Xie, H.W.; Xing, P.F.; Wang, D.H.; Yin, H.Y. A self-driven alloying/dealloying approach to nanostructuring micro-silicon for high-performance lithium-ion battery anodes. *Energy Storage Mater.* **2021**, *34*, 768–777. [CrossRef]
51. Yuan, J.; Gan, Y.; Xu, X.; Mu, M.; He, H.; Li, X.; Zhang, X.; Liu, J. Construction of Fe₇Se₈@Carbon nanotubes with enhanced sodium/potassium storage. *J. Colloid Interface Sci.* **2022**, *626*, 355–363. [CrossRef] [PubMed]
52. Augustyn, V.; Simon, P.; Dunn, B. Pseudocapacitive oxide materials for high-rate electrochemical energy storage. *Energy Environ. Sci.* **2014**, *7*, 1597–1614. [CrossRef]
53. Song, J.; Ji, Y.; Li, Y.; Lu, X.; Ren, W.; Tian, Q.; Chen, J.; Yang, L. Porous carbon assisted carbon nanotubes supporting Fe₃O₄ nanoparticles for improved lithium storage. *Ceram. Int.* **2021**, *47*, 26092–26099. [CrossRef]
54. Wang, F.M.; Alemu, T.; Yeh, N.H.; Wang, X.C.; Lin, Y.W.; Hsu, C.C.; Chang, Y.J.; Liu, C.H.; Chuang, C.I.; Hsiao, L.H.; et al. Interface Interaction Behavior of Self-Terminated Oligomer Electrode Additives for a Ni-Rich Layer Cathode in Lithium-Ion Batteries: Voltage and Temperature Effects. *ACS Appl. Mater. Interfaces* **2019**, *11*, 39827–39840. [CrossRef]
55. Wu, H.B.; Chen, J.S.; Hng, H.H.; Lou, X.W. Nanostructured metal oxide-based materials as advanced anodes for lithium-ion batteries. *Nanoscale* **2012**, *4*, 2526–2542. [CrossRef]
56. Bal, B.; Ozdogru, B.; Nguyen, D.T.; Li, Z.; Murugesan, V.; Çapraz, Ö.Ö. Probing the Formation of Cathode-Electrolyte Interphase on Lithium Iron Phosphate Cathodes via Operando Mechanical Measurements. *ACS Appl. Mater. Interfaces* **2023**, *15*, 42449–42459. [CrossRef]
57. Zhang, H.; Zong, P.; Chen, M.; Jin, H.; Bai, Y.; Li, S.; Ma, F.; Xu, H.; Lian, K. In Situ Synthesis of Multilayer Carbon Matrix Decorated with Copper Particles: Enhancing the Performance of Si as Anode for Li-Ion Batteries. *ACS Nano* **2019**, *13*, 3054–3062. [CrossRef]